Observation of Unconventional Charge Density Wave without Acoustic Phonon Anomaly in Kagome Superconductors AV_3Sb_5 ($A = \mathrm{Rb}$, Cs)

Haoxiang Li,[1] T. T. Zhang,[2,3] T. Yilmaz,[4] Y. Y. Pai,[1] C. E. Marvinney,[1] A. Said,[5] Q. W. Yin,[6] C. S. Gong,[6] Z. J. Tu,[6] E. Vescovo,[4] C. S. Nelson,[4] R. G. Moore,[1] S. Murakami,[2,3] H. C. Lei,[6,*] H. N. Lee,[1] B. J. Lawrie,[1] and H. Miao[1,†]

[1]*Materials Science and Technology Division, Oak Ridge National Laboratory, Oak Ridge, Tennessee 37831, USA*
[2]*Department of Physics, Tokyo Institute of Technology, Okayama, Meguro-ku, Tokyo 152-8551, Japan*
[3]*Tokodai Institute for Element Strategy, Tokyo Institute of Technology, Nagatsuta, Midori-ku, Yokohama, Kanagawa 226-8503, Japan*
[4]*National Synchrotron Light Source II, Brookhaven National Laboratory, Upton, New York 11973, USA*
[5]*Advanced Photon Source, Argonne National Laboratory, Argonne, Illinois 60439, USA*
[6]*Department of Physics and Beijing Key Laboratory of Opto-Electronic Functional Materials and Micro-devices, Renmin University of China, Beijing, China*

(Received 24 March 2021; revised 15 May 2021; accepted 1 July 2021; published 3 September 2021)

The combination of nontrivial band topology and symmetry-breaking phases gives rise to novel quantum states and phenomena such as topological superconductivity, quantum anomalous Hall effect, and axion electrodynamics. Evidence of intertwined charge density wave (CDW) and superconducting order parameters has recently been observed in a novel kagome material AV_3Sb_5 (A = K, Rb, Cs) that features a $\mathbb{Z}_2$ topological invariant in the electronic structure. However, the origin of the CDW and its intricate interplay with the topological state has yet to be determined. Here, using hard-x-ray scattering, we demonstrate a three-dimensional CDW with $2 \times 2 \times 2$ superstructure in $(\mathrm{Rb}, \mathrm{Cs})V_3Sb_5$. Unexpectedly, we find that the CDW fails to induce acoustic phonon anomalies at the CDW wave vector but yields a novel Raman mode that quickly damps into a broad continuum below the CDW transition temperature. Our observations exclude strong electron-phonon-coupling-driven CDW in AV_3Sb_5 and support an unconventional CDW that was proposed in the kagome lattice at van Hove filling.

DOI: 10.1103/PhysRevX.11.031050 Subject Areas: Condensed Matter Physics

I. INTRODUCTION

The charge density wave (CDW), a translational symmetry-breaking electronic fluid, plays a crucial role in unconventional superconductors and intertwined electronic orders [1–5]. While CDWs have been isolated from topological excitations, recently experimental evidence of a topological CDW with chiral flux has been observed in a new kagome metal AV_3Sb_5 (A = K, Rb, Cs) [6], whose crystal structure and 3D Brillouin zone are shown in Figs. 1(a) and 1(b), respectively. Density-functional-theory (DFT) calculations of the electronic structure find a $\mathbb{Z}_2$ topological invariant and an electronic filling close to van Hove singularity (saddle point) near the M point [7,8]. Because of the frustrated lattice structure and sublattice interference effect, unconventional p-wave CDW and chiral flux phase have been theoretically predicted near the van Hove filling [4,9–11]. Moreover, the CDW in AV_3Sb_5 may intertwine with the superconductivity at low temperature and give rise to the possible roton pair-density wave and Majorana zero mode [12,13]. Despite the intimate correlations between the CDW, superconductivity, and topological band structure [6–8,11–18], the nature of the CDW, in particular, its interplay with the lattice degree of freedom, remains largely unexplored. This knowledge gap hinders the understanding of unconventional Fermi-surface instabilities in kagome metals near van Hove filling.

Theoretically, the CDW mechanisms are broadly separated into two categories: weak-coupling scenarios based on Fermi-surface instabilities [19–21] and strong-coupling theories derived from local electron-electron or electron-phonon interactions [22–25]. As we show in Figs. 1(c) and 1(d), due to the finite electron-phonon coupling (EPC), the formation of CDWs distorts the underlying lattice and typically results in acoustic phonon anomalies. For a weak-coupling mechanism, the phonon softening is sharply confined near the CDW wave vector $\mathbf{Q}_{\mathrm{CDW}}$ and is known as the Kohn anomaly [21] [illustrated in Fig. 1(e)]. In

*hlei@ruc.edu.cn
†miaoh@ornl.gov

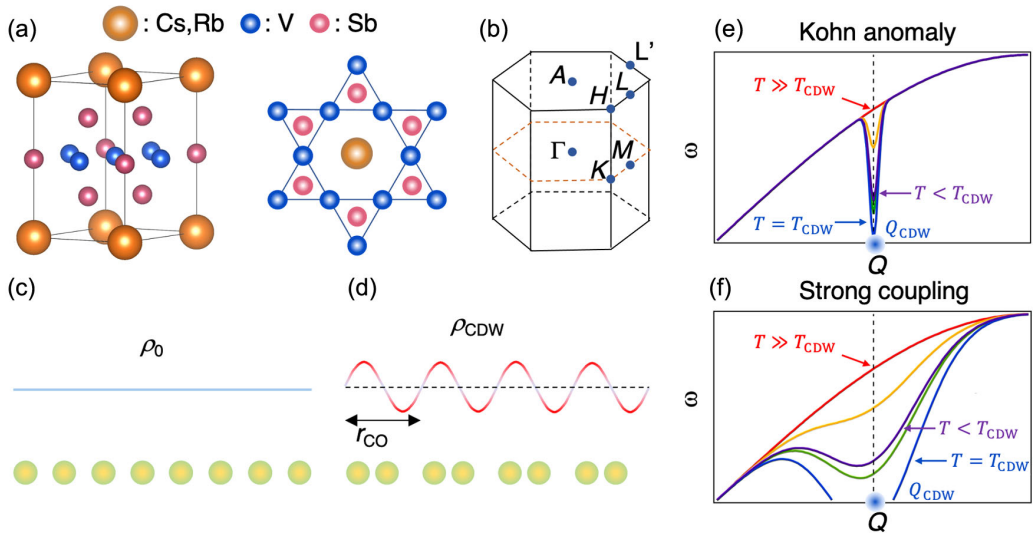

FIG. 1. The crystal structure of AV_3Sb_5 and CDW-induced phonon anomalies. (a) shows the crystal structure of AV_3Sb_5 (space group $P6/mmm$, no. 191), which consists of V-Sb slabs that are separated by alkali elements. The V-Sb slab contains a V-kagome lattice and two Sb sites laying in the kagome plane and above the V triangle. (b) shows the 3D BZ and high-symmetry points of AV_3Sb_5. (c) and (d) show the valence and core electron density in the normal and CDW phase, respectively. Because of EPC, the core electrons will follow the CDW period and yield acoustic phonon anomalies. (e) Nesting-induced Kohn anomalies. (f) Strong-coupling-induced phonon softening in an extended momentum space near $\mathbf{Q}_{CDW}$. Red, yellow, green, blue, and purple colors represent temperatures from $T \gg T_{CDW}$ to $T < T_{CDW}$. The phonon hardening for $T < T_{CDW}$ is due to the CDW amplitude mode.

contrast, strong-coupling mechanisms usually give rise to phonon anomalies in an extended $\mathbf{Q}$ range near $\mathbf{Q}_{CDW}$ [26–29], as shown in Fig. 1(f). Comparing with previously explored CDW systems, the kagome structure has a unique sublattice interference effect, which may give rise to unconventional Fermi-surface instabilities that carry finite angular momentum [11,30]. How lattice excitations interact with the finite-angular-momentum CDW remains unresolved. Here we combine inelastic x-ray scattering (IXS), Raman spectroscopy, and angle-resolved photoemission spectroscopy (ARPES) to show evidence of a novel electronic driven CDW in AV_3Sb_5 ($A = \mathrm{Cs, Rb}$). We demonstrate that the bulk CDW has three-dimensional (3D) $2 \times 2 \times 2$ superstructure, which fails to induce longitudinal-acoustic (LA) and transverse-acoustic (TA) phonon anomalies. The absence of acoustic phonon anomaly firmly excludes strong electron-phonon-driven CDW. Interestingly, we discover a novel Raman mode that emerges at the CDW temperature T_{CDW} and is quickly damped below T_{CDW} into a continuum that broadly peaks at 20 meV. Our results uncover the intriguing nature of the CDW phase in AV_3Sb_5 and shed light on the intertwined electronic and lattice instabilities in kagome metal near the van Hove filling.

II. THREE-DIMENSIONAL $2 \times 2 \times 2$ SUPERSTRUCTURE

We first determine the bulk CDW superlattice peaks using meV-resolution XRD. Figures 2(a) and 2(b) show the temperature-dependent L scan of RbV_3Sb_5 at $\mathbf{Q} = (3.5, 0, 0)$ and $(3.5, 0, 0.5)$ in reciprocal lattice units (r.l.u.). The onset temperature at $T = 103 \pm 0.5$ K is consistent with the CDW transition temperature in RbV_3Sb_5 (see the Appendix A). The absence of hysteresis, as shown in Figs. 2(c) and 2(d), supports a second-order or a weak first-order phase transition. The observation of a CDW peak at half integer L in Fig. 2(b) proves that the CDW in RbV_3Sb_5 forms a 3D $2 \times 2 \times 2$ superstructure rather than a 2D 2×2 superstructure as suggested by early STM and XRD measurements [6,8,13,16] and consistent with a recent STM work that shows a π phase shift of the in-plane CDW between stacking layers [12]. Interestingly, as shown in Fig. 2(a) ($L = 0$) and Fig. 2(b) ($L = 0.5$), the up-turn slopes of the CDW peak intensity are different, suggesting the coexistence of different electronic orders [17] or different stacking schemes [31]. It should be noted that CDW peaks at $L = 0$ and 0.5 have different sensitivity to atomic distortions, which may also be related to different up-turn slopes. By fitting the CDW peak with a Lorenzian-squared function [32,33], we find that the CDW correlation length defined as the inverse half width at half maximum (1/HWHM) is larger than 500 Å along the L direction, establishing a long-range-ordered 3D CDW. As shown in Figs. 2(e) and 2(f), the same 3D CDW superlattice structure is also observed in CsV_3Sb_5, suggesting a ubiquitous CDW mechanism for all AV_3Sb_5. We note that the CDW peaks in CsV_3Sb_5 are over twice broader than those of RbV_3Sb_5, which might be due to the larger stacking fault in CsV_3Sb_5 (see Supplemental Material [31]). Interestingly, we find that

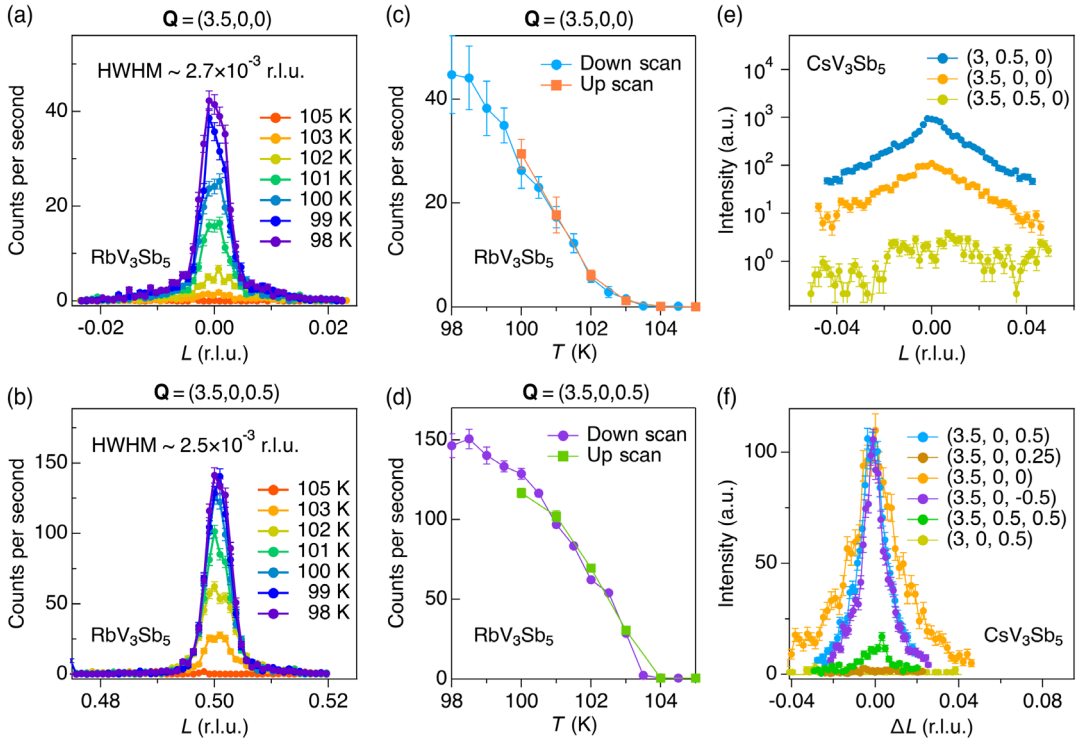

FIG. 2. 3D CDW determined by meV-resolution XRD. (a),(b) The temperature-dependent CDW peaks of RbV_3Sb_5 at $\mathbf{Q} = (3.5, 0, 0)$ and (3.5, 0, 0.5). The CDW peak at half-integer L demonstrates a 3D CDW with $2 \times 2 \times 2$ superstructure. The CDW peaks are extremely sharp along L, with HWHM of approximately 0.0025 r.l.u. at $T = 98$ K. (c) and (d) show the extracted temperature-dependent CDW peak intensity at $\mathbf{Q} = (3.5, 0, 0)$ and (3.5,0,0.5), respectively. The peak intensity takes a sharp upturn at the CDW onset temperature of 103 K for RbV_3Sb_5, which is consistent with the specific heat measurement (see Appendix A). The absence of hysteresis is consistent with a second-order phase transition. CDW peaks in CsV_3Sb_5 are shown in (e) and (f). The peak intensity at $\mathbf{Q} = (3, 0.5, 0)$ is over 10 times larger than the one at $\mathbf{Q} = (3.5, 0, 0)$ [panel (e)], consistent with larger structure factors at $\mathbf{Q} = (H, K + 0.5, 0)$, $H =$ odd integer [8]. The absence of peaks at $\mathbf{Q} = (3, 0, 0.5)$, (3.5, 0.5, 0), (3.5, 0, 0.25) confirms the same $2 \times 2 \times 2$ superstructure in CsV_3Sb_5. The error bars in panels (a),(b),(e),(f) represent 1 standard deviation assuming Poisson counting statistics. The error bars in panels (c) and (d) denote the 2σ returned from the pseudo-Voigt fittings that extract the peak intensity.

while the CDW is long-range ordered, the integrated CDW intensity that is proportional to the square of the lattice distortion is extremely small. Comparing with fundamental Bragg peaks, the CDW peak intensity is 3–5 orders of magnitude weaker, demonstrating small lattice distortions. An important consequence of the 3D $2 \times 2 \times 2$ superstructure is that it breaks the rotational symmetry from C_6 to C_2 [34]. This result thus indicates that the STM-observed C_6 symmetry breaking is likely a structural effect rather than electronic nematicity.

III. ABSENCE OF ACOUSTIC PHONON ANOMALY

With the 3D CDW established, we explore the origin of the CDW in AV_3Sb_5 using IXS and Raman spectroscopy. As we show in Fig. 1, the formation of CDWs is always accompanied by acoustic phonon anomalies because of EPC. Indeed, even in the cuprates, where CDWs are short ranged and possibly dynamical, a 15% LA phonon softening has been observed [26,27], demonstrating the acoustic phonon is a sensitive probe of CDW correlations. DFT calculation of the phonon dispersion of AV_3Sb_5 shows large negative frequency near the M and L points at zero temperature [15,31], indicating strong electron-phonon-coupling-induced CDW in AV_3Sb_5 [28,29,35,36]. To test this scenario, we perform IXS measurement along (3,0,0)–(3.5,0,0) and (3,3,0)–(3.5,2.5,0) to selectively enhance LA and TA phonon modes in our experimental geometry (see Ref. [31]). Unexpectedly, as we show in Figs. 3(a)–3(e), CDWs in AV_3Sb_5 fail to induce phonon anomalies on both TA and LA modes from $T = 300$ K $> T_{CDW}$ to 50 K $< T_{CDW}$. We note that in Fig. 3(d), beside the LA peaks at 12 meV, there is a low-energy peak at 7 meV in the spectra. This low-energy peak is the leakage signal of the TA mode as it locates at the same energy of the TA peak shown in Fig. 3(e). This 7-meV mode also presents an intensity enhancement at the low temperature similar to the TA peak. The intensity change below T_{CDW} is likely due to the CDW-induced lattice distortion that modifies the dynamic structure factor [37]. For the same reason, the 13-meV phonon mode shown in Fig. 3(e) also changes below T_{CDW}. The absence of phonon softening thus excludes strong EPC as the driving force of the CDW in AV_3Sb_5.

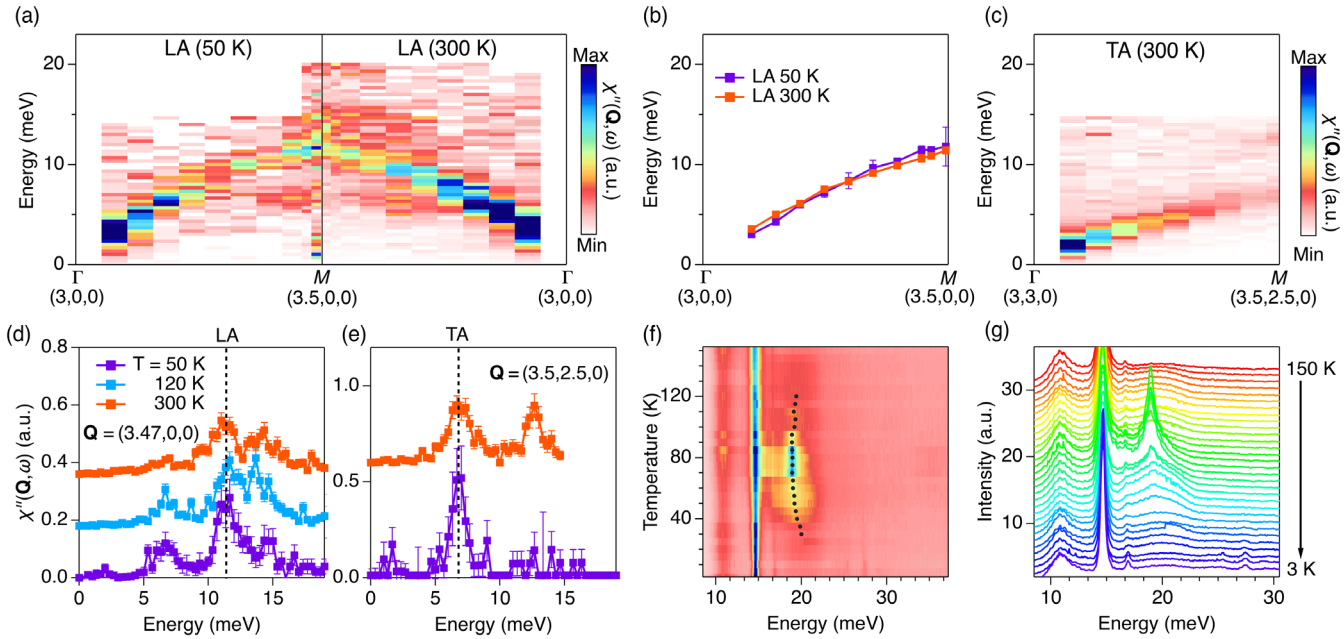

FIG. 3. Evidence of unconventional electronically driven CDW. (a) compares the IXS determined LA of RbV_3Sb_5 along $\Gamma(3,0,0)$ to $M(3.5,0,0)$ at temperatures of $T = 300$ K and 50 K ($T_{CDW} = 103$ K). (b) Extracted-temperature-dependent phonon dispersions from (a). (c) TA in RbV_3Sb_5 measured along $\Gamma(3,3,0)$ to $M(3.5,2.5,0)$ at room temperature (300 K). (d) and (e) compare temperature-dependent IXS spectra at $\mathbf{Q} = (3.47,0,0)$ and (3.5,2.5,0). The dashed lines in (d) and (e) highlight LA and TA, respectively. All IXS data are Bose-factor corrected, and the elastic contribution at $\omega = 0$ is subtracted by fitting the IXS raw data (see Supplemental Material [31]). (f),(g) Temperature-dependent Raman spectra on CsV_3Sb_5 from 150 to 3 K. Beside the sharp optical phonon peak at 11, 15, and 17 meV, there is a continuum that is broadly centered near 19 meV (the 11-meV peak may actually be at lower energy but appears to be at 11 meV due to the cutoff of the longpass filter at 11 meV). The black dots in (f) mark the peak positions of the continuum near 19 meV. When cooling toward T_{CDW}, the center of this continuum gradually shifts from 19.5 to 19 meV and starts to build a strong, sharp, and asymmetric peak at $T_{CDW} = 94$ K. Moving to lower temperature, this peak is quickly damped and hardened to 20 meV at 30 K. Below 30 K, two new phonon modes at 25.4 and 27.5 meV are observed, which may correspond to the stripe phase observed by a recent STM study [16]. The error bars in panels (d),(e) represent 1 standard deviation assuming Poisson counting statistics. The error bars in panel (b) denote the 2σ returned from the fitting that extracts the spectral peak position.

IV. EVIDENCE OF GAPPED CDW PHASE MODE

Raman spectroscopy provides further insight into the origin of CDW. Figures 3(f) and 3(g) show temperature-dependent Raman spectra of CsV_3Sb_5 with $T_{CDW} = 94$ K. According to DFT calculations (see Supplemental Material in [31]), four Raman active modes at 8.6, 15.1, 16.2, and 17.4 meV corresponding to the E_{1g}, E_{2g}, A_{1g}, and B_{2g} modes, respectively, are allowed for the normal-state structure. At 150 K, we observe three optical phonon modes at 11, 15, and 17 meV, which we attribute to the E_{1g}, E_{2g}, and B_{2g} modes (the 11-meV peak may actually be at lower energy but appears to be at 11 meV due to the cutoff of the longpass filter at 11 meV). Interestingly, we observe a continuum that is broadly centered around 19.5 meV. As we cool down toward the T_{CDW}, the center of this continuum gradually shifts to lower energy and eventually develops into a strong, sharp, and asymmetric peak at 19 meV, demonstrating its intimate correlation with the CDW. Unexpectedly, moving to a lower temperature, the intensity of this peak is suppressed. Remarkably, this unconventional mode shows clear softening above T_{CDW} and hardening below T_{CDW}, reminiscent of the CDW phason and amplitudon excitations near the $\mathbf{Q}_{CDW}$ [28,29,31,38–40]. A similar effect near the Brillouin zone center has been observed in CDW material $TiSe_2$ [29], which also has a 3D $2 \times 2 \times 2$ superstructure. The temperature-dependent Raman mode together with the absence of an acoustic phonon anomaly suggest that the CDW in AV_3Sb_5 might be a novel realization of particle-hole condensation in a metallic system, where the particle-hole excitation is highly damped by itinerant electrons. In this scenario, the absence of phonon softening might be a signature of a large CDW phason gap that is induced by the commensurability effect [41]. As we discuss in more detail in Appendix B, for commensurate CDW, the phason gap can be expressed as [41]

$$\omega_\phi \sim \Delta \left(\frac{\Delta}{D}\right)^{(M-2)/2}, \tag{1}$$

where D is the electronic bandwidth, Δ is the CDW gap, and M is the CDW period relative to the lattice constant a_0. Usually, the bandwidth $D \gg \Delta$ and therefore, $\omega_\phi \sim 0$.

However, for CDW period $M = 2$, which is the case for AV_3Sb_5, $\omega_\phi \sim \Delta$. Besides the commensurability effect, a weak first-order phase transition as suggested by recent nuclear-magnetic- and quadruple-resonance measurements [42,43] may also be responsible for the absence of the acoustic phonon anomaly. DFT calculations suggest that the inverse start-of-David distortion corresponding to an unstable optical phonon is the energetically favored structure in the CDW phase [15]. While the softening of the optical phonon is expected to induce LA phonon anomalies (see Supplemental Material [31]), the weak first-order phase transition in AV_3Sb_5 may yield a discontinuous and small modification of LA that is not resolved by our measurement.

Below 30 K, we observe additional Raman active modes at 25.4 and 27.5 meV, demonstrating an additional symmetry-breaking phase at low temperature. Comparing with a previous STM study [16], this new low-temperature phase is possibly the unidirectional CDW. Interestingly, this new symmetry-breaking phase correlates strongly with the CDW-related continuum, where the intensity of the continuum significantly suppresses when the new Raman modes emerge.

V. SADDLE POINT AND QUASI-NESTED ELECTRON AND HOLE POCKETS

To disclose the particle-hole scattering channel that is connected by the 3D CDW, in Fig. 4, we show the low-temperature ($T = 15$ K) electronic structure of RbV_3Sb_5 determined by ARPES measurements and DFT calculations. As shown in Figs. 4(a) and 4(b), the overall Fermi-surface topology is similar to previous ARPES studies of KV_3Sb_5 and CsV_3Sb_5 [8,44], hence, confirming the ubiquitous van Hove filling of AV_3Sb_5. Photon energies of $h\nu = 100$ and 90 eV correspond to $k_z = \pi$ and 0.15π around the $\bar{M}$ point, respectively (see Supplemental Material [31] for the k_z map). The most important observations are shown in Figs. 4(c) and 4(d) corresponding to the blue cut in Figs. 4(a) and 4(b), respectively. At $k_z = \pi$, we observe a shallow electron band with a band bottom of approximately 50 meV, while at $k_z = 0.15\pi$, we observe a steep holelike band dispersing toward the Fermi level. The shallow electron and hole band can be further revealed by the stacking momentum-distribution curves (MDCs) displayed in Figs. 4(e) and 4(f). Similar electronic structure is also observed in CsV_3Sb_5 (see Supplemental Material

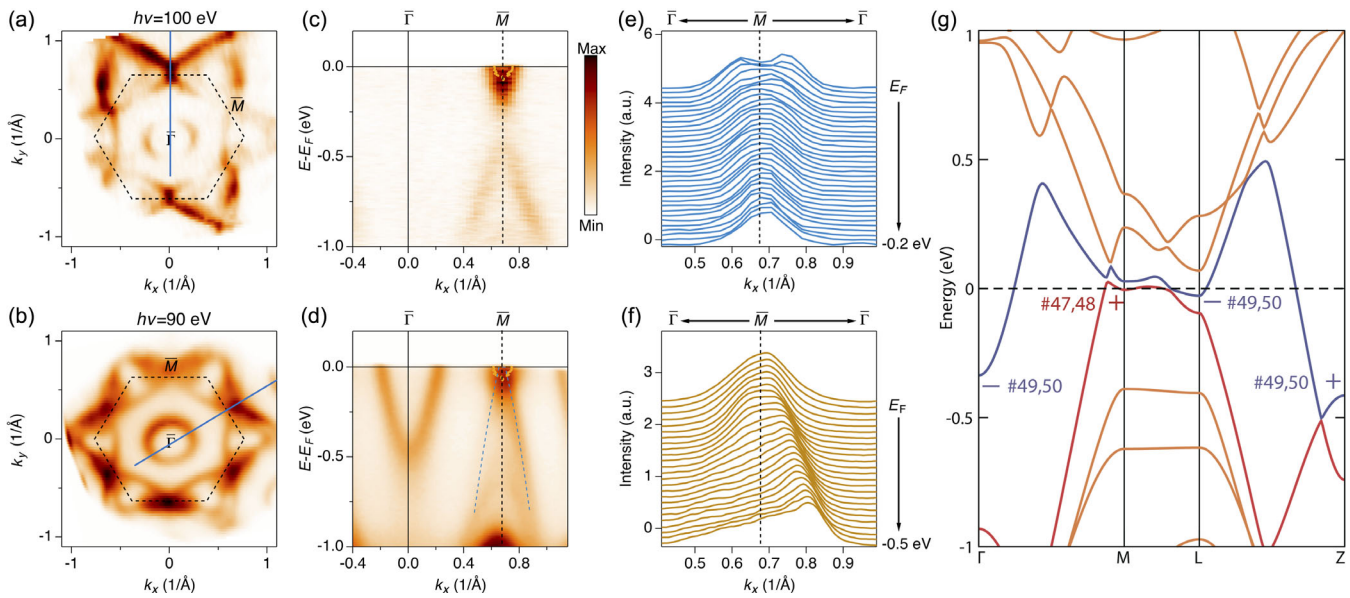

FIG. 4. 3D-CDW-induced band inversion. (a) and (b) show Fermi-surface maps measured at photon energies of $h\nu = 100$ and 90 eV corresponding to $k_z = \pi$ and 0.15π around the $\bar{M}$ point, respectively. Data are taken at $T = 15$ K. The blue lines in (a) and (b) mark the high-symmetry cuts shown in (c) and (d), respectively. The inner potential is extracted to be around 8.2 eV (see Supplemental Material [31]). (c) and (d) selectively enhance the electron band near the unfolded L point and the hole band near the unfolded M point. The yellow dots in (c) and (d) are extracted from the MDC peaks shown in (e). The blue dashed line in (d) is a guide to the eye. The blurry spectral weight near the Fermi level in (d) likely comes from the bulk projected surface state [8]. (e) and (f) show stacking plots of MDCs to further reveal the electron and hole bands in panels (c) and (d). (g) shows the electronic band structure of RbV_3Sb_5 calculated by VASP [45–47] after a full relaxation on atomic positions with an atom pairwise-correction method (DFT-D3) [48] since the van der Waals forces play an important role along the c-layer stacking direction. The Fermi energy is shifted by 100 meV in order to match the experimental results. There is a hole pocket in the vicinity of the M point (Γ-M direction) carrying a parity of "+" and an electron pocket in the vicinity of the L point carrying a parity of "−" contributed by different bands. Our DFT result confirms the parity distribution of the band structure that is reported to possess a nontrivial $\mathbb{Z}_2$ topological invariant and induce topological surface states around the M point [8].

[31]). Our observations establish two particle-hole channels that are possibly relevant to the CDW: (i) the saddle points at the M point [4,5,11,15] and (ii) the quasinested electron and hole pockets at the M and L points [see Fig. 1(b)]. Because of the high density of state of the saddle point, the leading Fermi-surface instability, if any, should be driven by the saddle point [5,11,30,42], while the electron-hole nesting may help to stabilize the L component of the 3D CDW. We note, however, that the electronic structure near the M point [Fig. 4(d)] is not fully captured by the DFT calculations of the ideal kagome structure shown in Fig. 4(g), which might be due to surface effects [8] or a number of stacking faults in AV_3Sb_5 (see Supplemental Material [31]).

VI. CONCLUSION

In summary, we demonstrate an unconventional 3D CDW in the $\mathbb{Z}_2$ kagome superconductor AV_3Sb_5, where the formation of CDW fails to induce phonon anomalies near $\mathbf{Q}_{\mathrm{CDW}}$. Our observations exclude strong EPC-driven CDW in AV_3Sb_5 and point to an unconventional CDW phase in an intertwined electronic state.

ACKNOWLEDGMENTS

We thank J. G. Cheng, Y. M. Dai, R. Thomale, Z. Q. Wang, Z. Y. Wang, S. F. Wu, B. H. Yan, and J. X. Yin for stimulating discussions. This research is sponsored by the U.S. Department of Energy, Office of Science, Basic Energy Sciences, Materials Sciences and Engineering Division (ARPES experiment and Raman spectroscopy) and by the Laboratory Directed Research and Development Program of Oak Ridge National Laboratory managed by UT-Battelle, LLC, for the U.S. Department of Energy (IXS and XRD experiment). This research uses resources (IXS experiment at beam line 30ID) of the Advanced Photon Source, a U.S. DOE Office of Science User Facility operated for the DOE Office of Science by Argonne National Laboratory under Contract No. DE-AC02-06CH11357. Hard-x-ray diffraction and ARPES measurements use resources at the 4-ID and 21-ID-1 beam lines of the National Synchrotron Light Source II, a U.S. Department of Energy Office of Science User Facility operated for the DOE Office of Science by Brookhaven National Laboratory under Contract No. DE-SC0012704. Extraordinary facility operations are supported in part by the DOE Office of Science through the National Virtual Biotechnology Laboratory, a consortium of DOE national laboratories focused on the response to COVID-19, with funding provided by the Coronavirus CARES Act. Raman spectroscopy is conducted at the Center for Nanophase Materials Sciences, which is a DOE Office of Science User Facility. T. T. Z. and S. M. acknowledge support from Tokodai Institute for Element Strategy funded by MEXT Elements Strategy Initiative to Form Core Research Center. T. T. Z. and S. M. also acknowledge the supports from JSPS KAKENHI Grants No. JP18H03678 and No. JP20H04633. T. Z. also acknowledge the support from JSPS KAKENHI Grants No. JP21K13865. H. C. L. acknowledges the support from the National Key R&D Program of China (Grants No. 2016YFA0300504 and No. 2018YFE0202600), the National Natural Science Foundation of China (Grants No. 11774423 and No. 11822412), the Fundamental Research Funds for the Central Universities, and the Research Funds of Renmin University of China (Grants No. 18XNLG14 and No. 19XNLG17). C. M. is supported by the Intelligence Community Postdoctoral Research Fellowship Program at the Oak Ridge National Laboratory, administered by the Oak Ridge Institute for Science and Education through an interagency agreement between the U.S. Department of Energy and the Office of the Director of National Intelligence. H. C. L. is supported by National Natural Science Foundation of China (Grants No. 11822412 and No. 11774423), Ministry of Science and Technology of China (Grants No. 2018YFE0202600 and No. 2016YFA0300504), and Beijing Natural Science Foundation (Grant No. Z200005).

Note added.—Recently, the CDW gap Δ_{CDW} was observed in ARPES [49,50] and optical studies [51] near the M point. This new observation does not contradict the absence of phonon anomaly. We note that the CDW gap opening can be a consequence of the $2 \times 2 \times 2$ superstructure, which induces band folding and gap opening.

APPENDIX A: METHODS

1. Sample

Single crystals of AV_3Sb_5 ($A = \mathrm{Rb}$, Cs) are grown from Rb ingot (purity 99.9%), Cs ingot (purity 99.9%), V powder (purity 99.9%), and Sb grains (purity 99.999%) using the self-flux method, similar to the growth of RbV_3Sb_5 [14]. The mixture is put into an alumina crucible and sealed in a quartz ampoule under partial argon atmosphere. The sealed quartz ampoule is heated to 1273 K for 12 h and soaks there for 24 h. Then it is cooled down to 1173 K at 50 K/h and further to 923 K at a slow rate. Finally, the ampoule is taken out from the furnace and decanted with a centrifuge to separate $(\mathrm{Cs,Rb})V_3Sb_5$

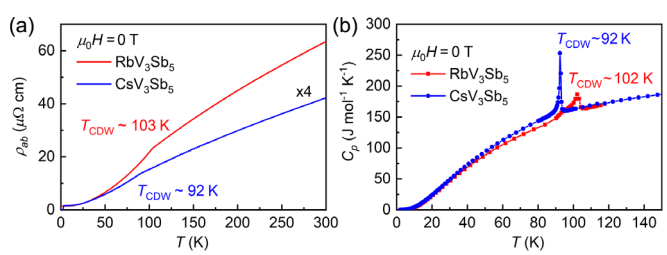

FIG. 5. (a) and (b) show transport and specific heat measurement of RbV_3Sb_5 (red) and CsV_3Sb_5 (blue).

single crystals from the flux. The obtained crystals have a typical size of $2 \times 2 \times 0.02$ mm^3. CDW transition is clearly observed in transport and specific heat measurement shown in Figs. 5(a) and 5(b), respectively.

2. Inelastic x-ray scattering

The experiments are conducted at beam line 30-ID-C (HERIX) at the Advanced Photon Source. The highly monochromatic x-ray beam of incident energy $E_i = 23.7$ keV ($\mathrm{l} = 0.5226$ Å) is focused on the sample with a beam cross section of 35×15 μm^2 (horizontal vertical). The total energy resolution of the monochromatic x-ray beam and analyzer crystals is $\Delta E \sim 1.5$ meV (full width at half maximum). The measurements are performed in transmission geometry. Typical counting times are in the range of 30 to 360 sec per point in the energy scans at constant momentum transfer $\mathbf{Q}$. H, K, L are defined in the hexagonal structure with $a = b = 5.472$ Å, $c = 9.073$ Å at room temperature for RbV_3Sb_5, and $a = b = 5.495$ Å, $c = 9.309$ Å at room temperature for CsV_3Sb_5.

3. Hard-x-ray diffraction

High-precision x-ray-scattering measurements are performed at the *in situ* and resonant 4-ID beam line of National Synchrotron Light Source II (NSLS-II). The photon energy, which is selected by a cryogenically cooled Si(111) double-crystal monochromator is 11.47 keV. The sample is mounted in a closed-cycle displex cryostat in a vertical scattering geometry, and the sigma-sigma scattering channel is measured using an MgO(440) polarization analyzer and silicon drift detector.

4. ARPES experiment

The ARPES experiments are performed on single crystals of RbV_3Sb_5 and CsV_3Sb_5. The samples are cleaved *in situ* in a vaccum better than 5×10^{-11} torr. The experiment is performed at beam line 21-ID-1 at the NSLS-II. The measurements are taken with synchrotron light source and a Scienta-Omicron DA30 electron analyzer. The total energy resolution of the ARPES measurement is approximately 15 meV. The sample stage is maintained at low temperature ($T = 15$ K) throughout the experiment.

5. Raman experiment

Raman spectroscopy is performed in a Montana Instruments closed-cycle cryostation s100 and utilize a Hubner Photonics 532-nm diode-pumped-laser excitation and an Isoplane SCT-320 imaging spectrograph with a 400B-eXcelon CCD camera and a 2400-groove/mm visible-holographic grating. Semrock dichroic and longpass filters are integrated in the optics train. For all Raman spectra reported here, a 2-mW laser-excitation power is used, and Raman spectra are acquired for 300 s each. The sample is initially cooled to 3 K then heated to 150 K. All of the reported Raman spectra are then acquired while monotonically recooling the sample from 150 to 3 K. The optics train is refocused at each temperature after waiting for the sample temperature to stabilize in order to correct for changes due to thermal expansion and to ensure that the sample is in thermal equilibrium before acquiring a spectrum.

6. DFT calculations

The electronic band structure of RbV_3Sb_5 is calculated by VASP [45–47] after a full relaxation on atomic positions with an atom pairwise-correction method (DFT-D3) [48]. The phonon band structure of RbV_3Sb_5 is calculated using VASP within the Perdew-Burke-Ernzerhof exchange correlation based on density-functional perturbation theory. An equivalent k-point mesh of $9 \times 9 \times 6$ is used in the self-consistent calculation, and the cutoff energy for the plane-wave basis is 400 eV. Prior to the phonon spectra calculation, crystal structure is relaxed with the residual force on each atom less than 0.001 eV/Å.

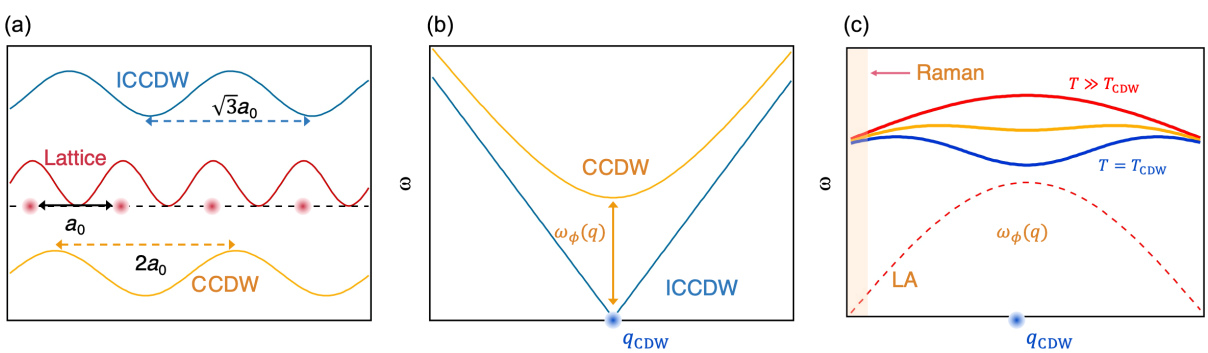

FIG. 6. (a) schematically shows commensurate (yellow) and incommensurate (cyan) CDW periods with respect to the lattice (red). (b) Yellow and cyan curves are the calculated phase modes for CCDW and ICCDW, respectively. (c) shows the CDW mechanism without electron-acoustic phonon interaction. The temperature-dependent particle-hole excitations are shown as red, yellow, and blue curves. The dashed line show the LA mode, whose energy at q_{CDW} is less than ω_ϕ. Shaded pink area indicates the momentum position of the Raman measurement.

APPENDIX B: COMMENSURABILITY EFFECT

For incommensurate CDW (ICCDW), the condensation energy E_{cond} is independent of the phase of CDW, ϕ. For commensurate CDW (CCDW), however, the condensation energy becomes phase dependent,

$$E_{\mathrm{cond}}(\phi) = -\frac{n(\epsilon_F)\Delta_{\mathrm{CDW}}^2}{\lambda}\left(\frac{\Delta}{D}\right)^{M-2}\cos(M\phi), \qquad \text{(B1)}$$

where λ is the dimensionless EPC constant, and $n(\epsilon_F)$ and Δ are the density of state at E_F and the CDW gap, respectively. M is the CDW period relative to the lattice constant a_0. D is the electronic bandwidth. This phase-dependent $E_{\mathrm{cond}}(\phi)$ means that gliding the CDW requires finite energy corresponding to a finite gap in the CDW phase mode

$$\omega_\phi(q) = \left(\frac{\omega_F^2}{M} + v_F^2\frac{m}{m^*}q^2\right)^{1/2}, \qquad \text{(B2)}$$

where $\omega_F^2 = (4M^2/\lambda)(m\Delta^2/m^*)(\Delta/D)^{M-2}m^*$. m^* is the effective mass. At $q = q_{\mathrm{CDW}}$, Eq. (B2) gives

$$\omega_\phi = \sqrt{\frac{4M}{\lambda}\frac{m}{m^*}}\Delta\left(\frac{\Delta}{D}\right)^{(M-2)/2}. \qquad \text{(B3)}$$

Usually, $D \gg \Delta$ and therefore, $\omega_\phi \sim 0$. However, for $M = 2$, which is the case for AV_3Sb_5, $\omega_\phi = \sqrt{(4M/\lambda)(m/m^*)}\Delta$. Interestingly, a simple parabolic fitting of the ARPES data shown in Fig. 4 gives $(m/m^*) \sim 3$ for the shallow electron and hole pockets, suggesting large ω_ϕ in AV_3Sb_5. As we show in Fig. 6(c), due to the large phason gap, the particle-hole condensation will not interact with acoustic phonon modes, as these modes are laying inside the phason gap.

[1] E. Fradkin, S. A. Kivelson, and J. M. Tranquada, *Colloquium: Theory of Intertwined Orders in High Temperature Superconductors*, Rev. Mod. Phys. **87**, 457 (2015).

[2] P. A. Lee, *Amperean Pairing and the Pseudogap Phase of Cuprate Superconductors*, Phys. Rev. X **4**, 031017 (2014).

[3] H. Miao, R. Fumagalli, M. Rossi, J. Lorenzana, G. Seibold, F. Yakhou-Harris, K. Kummer, N. B. Brookes, G. D. Gu, L. Braicovich, G. Ghiringhelli, and M. P. M. Dean, *Formation of Incommensurate Charge Density Waves in Cuprates*, Phys. Rev. X **9**, 031042 (2019).

[4] M. L. Kiesel, C. Platt, and R. Thomale, *Unconventional Fermi Surface Instabilities in the Kagome Hubbard Model*, Phys. Rev. Lett. **110**, 126405 (2013).

[5] W.-S. Wang, Z.-Z. Li, Y.-Y. Xiang, and Q.-H. Wang, *Competing Electronic Orders on Kagome Lattices at van Hove Filling*, Phys. Rev. B **87**, 115135 (2013).

[6] Y.-X. Jiang *et al.*, *Discovery of Topological Charge Order in Kagome Superconductor* KV_3Sb_5, Nat. Mater. (2021) https://doi.org/10.1038/s41563-021-01034-y.

[7] B. R. Ortiz, L. C. Gomes, J. R. Morey, M. Winiarski, M. Bordelon, J. S. Mangum, I. W. H. Oswald, J. A. Rodriguez-Rivera, J. R. Neilson, S. D. Wilson, E. Ertekin, T. M. McQueen, and E. S. Toberer, *New Kagome Prototype Materials: Discovery of* KV_3Sb_5, RbV_3Sb_5, *and* CsV_3Sb_5, Phys. Rev. Mater. **3**, 094407 (2019).

[8] B. R. Ortiz, S. M. L. Teicher, Y. Hu, J. L. Zuo, P. M. Sarte, E. C. Schueller, A. M. M. Abeykoon, M. J. Krogstad, S. Rosenkranz, R. Osborn, R. Seshadri, L. Balents, J. He, and S. D. Wilson, CsV_3Sb_5*: A* $\mathbb{Z}_2$ *Topological Kagome Metal with a Superconducting Ground State*, Phys. Rev. Lett. **125**, 247002 (2020).

[9] M. M. Denner, R. Thomale, and T. Neupert, *Analysis of Charge Order in the Kagome Metal* AV_3Sb_5 *(A = K, Rb, Cs)*, arXiv:2103.14045.

[10] M. L. Kiesel and R. Thomale, *Sublattice Interference in the Kagome Hubbard Model*, Phys. Rev. B **86**, 121105(R) (2012).

[11] X. Feng, K. Jiang, Z. Wang, and J. Hu, *Chiral Flux Phase in the Kagome Superconductor* AV_3Sb_5, Science bulletin **66**, 1384 (2021).

[12] Z. Liang, X. Hou, W. Ma, F. Zhang, P. Wu, Z. Zhang, F. Yu, J. J. Ying, K. Jiang, L. Shan, Z. Wang, and X. H. Chen, *Three-Dimensional Charge Density Wave and Robust Zero-Bias Conductance Peak inside the Superconducting Vortex Core of a Kagome Superconductor* CsV_3Sb_5, arXiv:2103.04760 [Phys. Rev. X (to be published)].

[13] H. Chen *et al.*, *Roton Pair Density Wave and Unconventional Strong-Coupling Superconductivity in a Topological Kagome Metal*, arXiv:2103.09188.

[14] Q. Yin, Z. Tu, C. Gong, Y. Fu, S. Yan, and H. Lei, *Superconductivity and Normal-State Properties of Kagome Metal* RbV_3Sb_5 *Single Crystals*, Chin. Phys. Lett. **38**, 037403 (2021).

[15] H. Tan, Y. Liu, Z. Wang, and B. Yan, *Charge Density Waves and Electronic Properties of Superconducting Kagome Metals*, Phys. Rev. Lett. **127**, 046401 (2021).

[16] H. Zhao, H. Li, B. R. Ortiz, S. M. L. Teicher, T. Park, M. Ye, Z. Wang, L. Balents, S. D. Wilson, and I. Zeljkovic, *Cascade of Correlated Electron States in a Kagome Superconductor* CsV_3Sb_5, arXiv:2103.03118.

[17] F. H. Yu, T. Wu, Z. Y. Wang, B. Lei, W. Z. Zhuo, J. J. Ying, and X. H. Chen, *Concurrence of Anomalous Hall Effect and Charge Density Wave in a Superconducting Topological Kagome Metal*, Phys. Rev. B **104**, L041103 (2021).

[18] K. Y. Chen, N. N. Wang, Q. W. Yin, Z. J. Tu, C. S. Gong, J. P. Sun, H. C. Lei, Y. Uwatoko, and J. G. Cheng, Double Superconducting Dome and Triple Enhancement of Tc in the Kagome Superconductor CsV_3Sb_5 under High Pressure Phys. Rev. Lett. **126**, 247001 (2021).

[19] M. D. Johannes and I. I. Mazin, *Fermi Surface Nesting and the Origin of Charge Density Waves in Metals*, Phys. Rev. B **77**, 165135 (2008).

[20] T. M. Rice and G. K. Scott, *New Mechanism for a Charge-Density-Wave Instability*, Phys. Rev. Lett. **35**, 120 (1975).

[21] M. Hoesch, A. Bosak, D. Chernyshov, H. Berger, and M. Krisch, *Giant Kohn Anomaly and the Phase Transition in Charge Density Wave* $ZrTe_3$, Phys. Rev. Lett. **102**, 086402 (2009).

[22] J. Zaanen and O. Gunnarsson, *Charged Magnetic Domain Lines and the Magnetism of High-*T_c *Oxides*, Phys. Rev. B **40**, 7391 (1989).

[23] K. Machida, *Magnetism in* La_2CuO_4 *based compounds*, Physica (Amsterdam) **158C**, 192 (1989).

[24] D. Poilblanc and T. M. Rice, *Charged Solitons in the Hartree-Fock Approximation to the Large-U Hubbard Model*, Phys. Rev. B **39**, 9749 (1989).

[25] C. M. Varma and A. L. Simons, *Strong-Coupling Theory of Charge-Density-Wave Transitions*, Phys. Rev. Lett. **51**, 138 (1983).

[26] H. Miao, D. Ishikawa, R. Heid, M. Le Tacon, G. Fabbris, D. Meyers, G. D. Gu, A. Q. R. Baron, and M. P. M. Dean, *Incommensurate Phonon Anomaly and the Nature of Charge Density Waves in Cuprates*, Phys. Rev. X **8**, 011008 (2018).

[27] M. Le Tacon, A. Bosak, S. M. Souliou, G. Dellea, T. Loew, R. Heid, K.-P. Bohnen, G. Ghiringhelli, M. Krisch, and B. Keimer, *Inelastic X-Ray Scattering in* $YBa_2Cu_3O_{6.6}$ *Reveals Giant Phonon Anomalies and Elastic Central Peak Due to Charge-Density-Wave Formation*, Nat. Phys. **10**, 52 (2014).

[28] F. Weber, S. Rosenkranz, J.-P. Castellan, R. Osborn, R. Hott, R. Heid, K.-P. Bohnen, T. Egami, A. H. Said, and D. Reznik, *Extended Phonon Collapse and the Origin of the Charge-Density Wave in* $2H$-$NbSe_2$, Phys. Rev. Lett. **107**, 107403 (2011).

[29] A. Kogar, M. S. Rak, S. Vig, A. A. Husain, F. Flicker, Y. I. Joe, L. Venema, G. J. MacDougall, T. C. Chiang, E. Fradkin, J. van Wezel, and P. Abbamonte, *Signatures of Exciton Condensation in a Transition Metal Dichalcogenide*, Science **358**, 1314 (2017).

[30] V. Thampy, S. Blanco-Canosa, M. Garcia-Fernandez, M. P. M. Dean, G. D. Gu, M. Först, T. Loew, B. Keimer, M. Le Tacon, S. B. Wilkins, and J. P. Hill, *Comparison of Charge Modulations in* $La_{1.875}Ba_{0.125}CuO_4$ *and* $YBa_2Cu_3O_{6.6}$, Phys. Rev. B **88**, 024505 (2013).

[31] See Supplemental Material at http://link.aps.org/supplemental/10.1103/PhysRevX.11.031050 for experimental details and additional data set.

[32] H. Miao, J. Lorenzana, G. Seibold, Y. Y. Peng, A. Amorese, F. Yakhou-Harris, K. Kummer, N. B. Brookes, R. M. Konik, V. Thampy, G. D. Gu, G. Ghiringhelli, L. Braicovich, and M. P. M. Dean, *High-Temperature Charge Density Wave Correlations in* $La_{1.875}Ba_{0.125}CuO_4$ *without Spin-Charge Locking*, Proc. Natl. Acad. Sci. U.S.A. **114**, 12430 (2017).

[33] H. Miao, G. Fabbris, R. J. Koch, D. G. Mazzone, C. S. Nelson, R. Acevedo-Esteves, G. D. Gu, Y. Li, T. Yilimaz, K. Kaznatcheev, E. Vescovo, M. Oda, T. Kurosawa, N. Momono, T. Assefa, I. K. Robinson, E. S. Bozin, J. M. Tranquada, P. D. Johnson, and M. P. M. Dean, *Charge Density Waves in Cuprate Superconductors beyond the Critical Doping*, npj Quantum Mater. **6**, 31 (2021).

[34] T. Park, M. Ye, and L. Balents, *Electronic Instabilities of Kagome Metals: Saddle Points and Landau Theory*, Phys. Rev. B **104**, 035142 (2021).

[35] C. Chen, B. Singh, H. Lin, and V. M. Pereira, *Reproduction of the Charge Density Wave Phase Diagram in* $1t$-$TiSe_2$ *Exposes Its Excitonic Character*, Phys. Rev. Lett. **121**, 226602 (2018).

[36] F. Weber, S. Rosenkranz, J.-P. Castellan, R. Osborn, G. Karapetrov, R. Hott, R. Heid, K.-P. Bohnen, and A. Alatas, *Electron-Phonon Coupling and the Soft Phonon Mode in* $TiSe_2$, Phys. Rev. Lett. **107**, 266401 (2011).

[37] A. Q. Baron, *Introduction to High-Resolution Inelastic X-Ray Scattering*, arXiv:1504.01098v2.

[38] J. P. Pouget, B. Hennion, C. Escribe-Filippini, and M. Sato, *Neutron-Scattering Investigations of the Kohn Anomaly and of the Phase and Amplitude Charge-Density-Wave Excitations of the Blue Bronze* $K_{0.3}MoO_3$, Phys. Rev. B **43**, 8421 (1991).

[39] S. Sugai, Y. Takayanagi, and N. Hayamizu, *Phason and Amplitudon in the Charge-Density-Wave Phase of One-Dimensional Charge Stripes in* $La_{2-x}Sr_xCuO_4$, Phys. Rev. Lett. **96**, 137003 (2006).

[40] D. H. Torchinsky, F. Mahmood, A. T. Bollinger, I. Božović, and N. Gedik, *Fluctuating Charge-Density Waves in a Cuprate Superconductor*, Nat. Mater. **12**, 387 (2013).

[41] P. Lee, T. Rice, and P. Anderson, *Conductivity from Charge or Spin Density Waves*, Solid State Commun. **14**, 703 (1974).

[42] C. Mu, Q. Yin, Z. Tu, C. Gong, H. C. Lei, Z. Li, and J. Luo, *s-Wave Superconductivity in Kagome Metal* CsV_3Sb_5 *Revealed by* $^{121/123}$Sb *NQR and* ^{51}V *NMR Measurements*, arXiv:2104.06698v1.

[43] D. W. Song, L. X. Zheng, F. H. Yu, J. Li, L. P. Nie, M. Shan, D. Zhao, S. J. Li, B. L. Kang, Z. M. Wu, Y. B. Zhou, K. L. Sun, K. Liu, X. G. Luo, Z. Y. Wang, J. J. Ying, X. G. Wan, T. Wu, and X. H. Chen, *Orbital Ordering and Fluctuations in a Kagome Superconductor* CsV_3Sb_5, arXiv:2104.09173.

[44] S.-Y. Yang, Y. Wang, B. R. Ortiz, D. Liu, J. Gayles, E. Derunova, R. Gonzalez-Hernandez, L. Šmejkal, Y. Chen, S. S. P. Parkin, S. D. Wilson, E. S. Toberer, T. McQueen, and M. N. Ali, *Giant, Unconventional Anomalous Hall Effect in the Metallic Frustrated Magnet Candidate,* Kv_3Sb_5, Sci. Adv. **6**, eabb6003 (2020).

[45] G. Kresse and J. Hafner, *Ab Initio Molecular-Dynamics Simulation of the Liquid-Metal–Amorphous-Semiconductor Transition in Germanium*, Phys. Rev. B **49**, 14251 (1994).

[46] G. Kresse and J. Furthmüller, *Efficient Iterative Schemes for Ab Initio Total-Energy Calculations Using a Plane-Wave Basis Set*, Phys. Rev. B **54**, 11169 (1996).

[47] G. Kresse and J. Furthmller, *Efficiency of Ab-Initio Total Energy Calculations for Metals and Semiconductors Using a Plane-Wave Basis Set*, Comput. Mater. Sci. **6**, 15 (1996).

[48] S. Grimme, S. Ehrlich, and L. Goerigk, *Effect of the Damping Function in Dispersion Corrected Density Functional Theory*, J. Comput. Chem. **32**, 1456 (2011).

[49] K. Nakayama, Y. Li, M. Liu, Z. Wang, T. Takahashi, Y. Yao, and T. Sato, *Multiple Energy Scales and Anisotropic Energy Gap in the Charge-Density-Wave Phase of Kagome Superconductor* CsV_3Sb_5, arXiv:2104.08042.

[50] R. Lou, A. Fedorov, Q. Yin, A. Kuibarov, Z. Tu, C. Gong, E. F. Schwier, B. Buchner, H. Lei, and S. Borisenko, *Charge-Density-Wave-Induced Peak-Dip-Hump Structure and Flat Band in the Kagome Superconductor* CsV_3Sb_5, arXiv:2106.06497.

[51] X. Zhou, Y. Li, X. Fan, J. Hao, Y. Dai, Z. Wang, Y. Yao, and H.-H. Wen, *Origin of the Charge Density Wave in the Kagome Metal* CsV_3Sb_5 *as Revealed by Optical Spectroscopy*, Phys. Rev. B **104**, L041101 (2021).